

# Multidimensional effects on proton acceleration using high-power intense laser pulses

K. D. Xiao,<sup>1</sup> C. T. Zhou,<sup>1,2,3, a)</sup> K. Jiang,<sup>4</sup> Y. C. Yang,<sup>1</sup> R. Li,<sup>1</sup> H. Zhang,<sup>2</sup> B. Qiao,<sup>1</sup> T. W. Huang,<sup>5</sup> J. M. Cao,<sup>3</sup> T. X. Cai,<sup>3</sup> M. Y. Yu,<sup>3</sup> S. C. Ruan,<sup>3,5</sup> and X. T. He<sup>1,2</sup>

<sup>1)</sup>*Center for Applied Physics and Technology, HEDPS, and School of Physics, Peking University, Beijing 100871, People's Republic of China*

<sup>2)</sup>*Institute of Applied Physics and Computational Mathematics, Beijing 100094, People's Republic of China*

<sup>3)</sup>*College of New Energy and New Materials, Shenzhen Technology University, Shenzhen 518118, People's Republic of China*

<sup>4)</sup>*Graduate School, China Academy of Engineering Physics, P.O. Box 2101, Beijing 100088, People's Republic of China*

<sup>5)</sup>*College of Optoelectronic Engineering, Shenzhen University, Shenzhen 518060, People's Republic of China*

(Dated: 24 May 2022)

Dimensional effects in particle-in-cell (PIC) simulation of target normal sheath acceleration (TNSA) of protons are considered. As the spatial divergence of the laser-accelerated hot sheath electrons and the resulting space-charge electric field on the target backside depend on the spatial dimension, the maximum energy of the accelerated protons obtained from three-dimensional (3D) simulations is usually much less than that from two-dimensional (2D) simulations. By closely examining the TNSA of protons in 2D and 3D PIC simulations, we deduce an empirical ratio between the maximum proton energies obtained from the 2D and 3D simulations. This ratio may be useful for estimating the maximum proton energy in realistic (3D) TNSA from the results of the corresponding 2D simulation. It is also shown that the scaling law also applies to TNSA from structured targets.

PACS numbers: 52.38.Kd, 52.65.Rr, 52.50.Jm, 29.25.-t

---

<sup>a)</sup>Electronic mail: [zcangtao@iapcm.ac.cn](mailto:zcangtao@iapcm.ac.cn)

## I. INTRODUCTION

Laser driven proton acceleration can produce proton beams of high energy and low divergence, as well as large proton number.<sup>1-5</sup> Such high-quality energetic proton beams are useful in ultrafast radiography, tumor therapy, inertial confinement fusion, etc.<sup>6-9</sup> The target normal sheath acceleration (TNSA) scheme is one of the most widely investigated mechanisms of proton acceleration.<sup>1,2,10-12</sup> In TNSA, the intense laser irradiating a thin solid target generates, heats, and accelerates the electrons on its front surface. The hot electrons can easily penetrate through the target and create a huge charge-separation electric field behind its rear surface, where protons can be accelerated by this electric field to a few or tens of MeV.<sup>13-17</sup>

Like in many experiments involving complex phenomena, in proton acceleration it is difficult to scan all the laser and target parameters due to the high operational cost and limited laser shots. With rapid development of computational techniques, parallelized computer simulations are useful for predicting and/or verifying experimental results and as guide for optimizing target design. However, full-scale three-dimensional (3D) particle-in-cell (PIC) simulations are at present still impractical if large regions and long times of interactions are involved, and two-dimensional (2D) simulations are often used instead. However, it has been found that the maximum proton energy (MPE) from 2D PIC simulations of TNSA is consistently overestimated compared with that from the 3D simulations and the experiments.<sup>18,19,21,44</sup> It is thus of interest to see if there exists a relation between the TNSA MPEs obtained from 2D and 3D simulations.

In this paper, we perform 2D and 3D PIC simulations of TNSA of protons under different conditions. By closely examining the results, we found a ratio of the MPEs from the 2D and 3D simulations. The empirical ratio is justified by a simple theoretical model and is consistent with that obtained from comparing the results from existing 2D simulations with the relevant experiments. Validity of this ratio for TNSA with micro-structured targets is also discussed.

The paper is arranged as follows. In Sec. II we compare the 2D and 3D results obtained from PIC simulations of femtosecond laser-driven TNSA proton acceleration. In Sec. III a model for the ratio of the 2D and 3D MPEs is introduced. In Sec. IV, the model is applied to picosecond-laser driven proton acceleration. Sec. V considers the dimensional effects on

TNSA using micro-structured targets. Sec. VI summarizes our results.

## II. PROTON ACCELERATION DRIVEN BY FEMTOSECOND LASER PULSES

The scheme for TNSA of protons is illustrated in Fig. 1(a). The target is assumed to be pre-ionized. A Gaussian laser pulse irradiates the foil target and the affected electrons on the target front are accelerated by the laser ponderomotive force. These hot electrons can transit through the foil target, so that an intense charge-separation electric field is created behind the foil's rear surface [see Figs. 1(b) and (c)]. The protons in a dot source attached to the latter are thereby accelerated by the intense charge-separation field. As can be seen in Figs. 1(b) and (c), the hot electrons and the sheath electric field behind the target are spatially divergent. Since the divergence is dimension dependent, there can be a difference in the results of the 2D and 3D PIC simulations of TNSA of protons.

To characterize the dimensional effects of TNSA of protons, two and three dimensional PIC simulations are carried out using the EPOCH2D and EPOCH3D PIC codes, respectively.<sup>22</sup> The flat foil target is composed of overdense copper plasma with electron number density  $n_0 = 40n_c$ , and particle collisions are neglected in the PIC simulations. (We have also carried out simulations for other electron densities and for both with and without particle collisions, but their effects on the resulting MPEs turn out to be small compared with that of the dimension.) The mass and charge of the copper ion are 63.5 and +2, respectively. The initial temperatures of the ions and electrons are  $T_i = 170$  eV and  $T_e = 1$  keV, respectively. The thickness and width of the target are  $1 \mu\text{m}$  and  $12 \mu\text{m}$ , respectively. A small-scale preplasma with the profile  $n_e = n_0 \exp(x/l)$ , where  $l = 0.3 \mu\text{m}$ , is placed in front of the target. A small proton dot of diameter  $1 \mu\text{m}$  and thickness  $0.5 \mu\text{m}$  providing the proton source is attached to the target backside.<sup>23–26</sup> A  $y$ -polarized Gaussian laser pulse with intensity  $1 \times 10^{21}$  W/cm<sup>2</sup> and wavelength 800 nm enters from the left boundary of the simulation box. The laser spot radius is  $3 \mu\text{m}$  and the pulse duration is 20 fs. In the 2D simulations, the simulation box is  $35 \mu\text{m}$  and  $20 \mu\text{m}$  in the  $x$  and  $y$  directions with 3279 and 1987 spatial grids, respectively. There are 50 electrons and 25 ions in each target cell. In the 3D simulations, the simulation box is  $35 \mu\text{m}$  and  $20 \mu\text{m}$  and  $20 \mu\text{m}$  in the  $x$ ,  $y$ , and  $z$  directions with 1640, 994, and 994 spatial grids, respectively. There are 4 electrons and 2 ions in each target cell. The corresponding

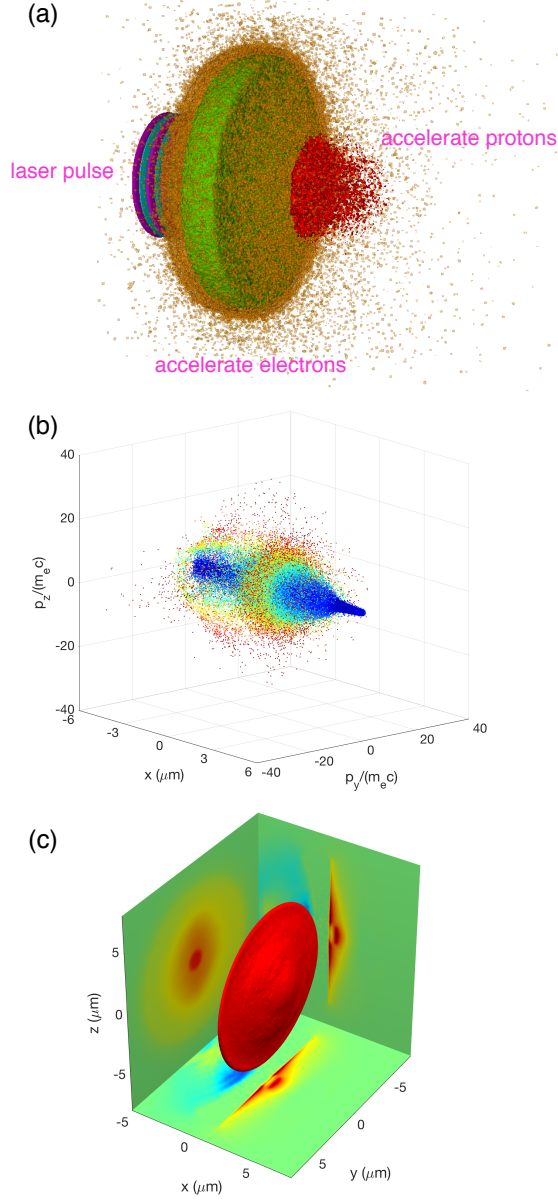


FIG. 1. (Color online) (a) Scheme for target normal sheath acceleration (TNSA) of protons. (b) Distribution of the transverse momentum ( $p_y$  and  $p_z$ ) of the accelerated electrons along the laser ( $x$ ) direction. (c) Averaged sheath electric field  $E_x$ .

grid length is 0.5 skin depth in the 2D and 1 skin depth in the 3D simulations. The proton dot in the 2D simulations is resolved by 47 spatial grids in the  $x$  direction and 99 spatial grids in the  $y$  direction. There are 500 proton macroparticles in each cell. The proton dot in the 3D simulations is resolved by 23 spatial grids in the  $x$  direction and 49 spatial grids in the  $y$ - and  $z$ -directions. There are 40 proton macroparticles in each cell. Periodic

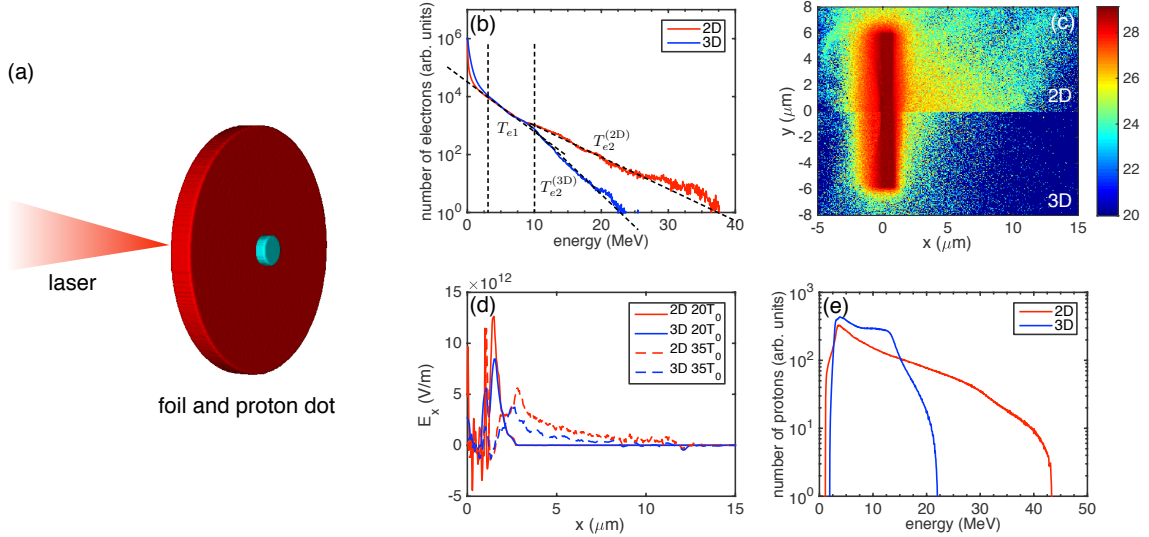


FIG. 2. (Color online) Simulation results for the flat foil target. (a) Target setup. (b) Electron spectrum at  $t = 30T_0$ . (c) Electron number density at  $t = 100T_0$ . (d) Profile of the electric field  $E_x$  at  $t = 20T_0$  and  $35T_0$ , respectively. (e) Proton spectrum at  $t = 100T_0$ .

boundary conditions are used in the transverse directions and open boundaries are used in the longitudinal directions. The laser enters from the left boundary of the box.

Figures 2 and 3 show the 2D and 3D simulation results. The electron energy spectrums are compared in Fig. 2(b). The electron number densities are shown in Fig. 2(c). As can be seen in Fig. 3, the divergence of the hot electrons is larger in 3D. The larger divergence in the 3D case reduces the electron recirculation rate inside the target, thereby weakening the electron heating. Fig. 2(b) shows that electrons with energies greater than 10 MeV as well as the maximum electron energy are lower in 3D than in 2D. Also, as shown in Figs. 2(b) and 2(c), the number of electrons with energies greater than 10 MeV as well as the electron number density, in the 3D case is smaller. Fig. 2(c) shows that due to the additional degree of freedom of the affected electrons, the laser hole boring depth in 3D is deeper than in 2D. According to the plasma expansion model of Mora,<sup>12</sup> the strength of the sheath field can be estimated by  $E_{\text{sheath}} = 2(4\pi n_e T_e)^{1/2} / (2e + \omega_{pi}^2 t^2)^{1/2}$ , where  $e = 2.71828$  is the Euler number and  $\omega_{pi} = (4\pi n_e e^2 / m_p)^{1/2}$  is the ion plasma frequency. Thus, the strength of the sheath field is  $\propto (n_e T_e)^{1/2}$ . Since both the electron number density and temperature are lower in 3D, the sheath electric field  $E_x$  at the target backside is weaker than that in 2D. In fact, we have [see Fig. 2 (d)]  $E_x^{(2D)} = 1.3 \times 10^{13}$  V/m and  $E_x^{(3D)} = 8 \times 10^{12}$  V/m at  $t = 20T_0$ ,

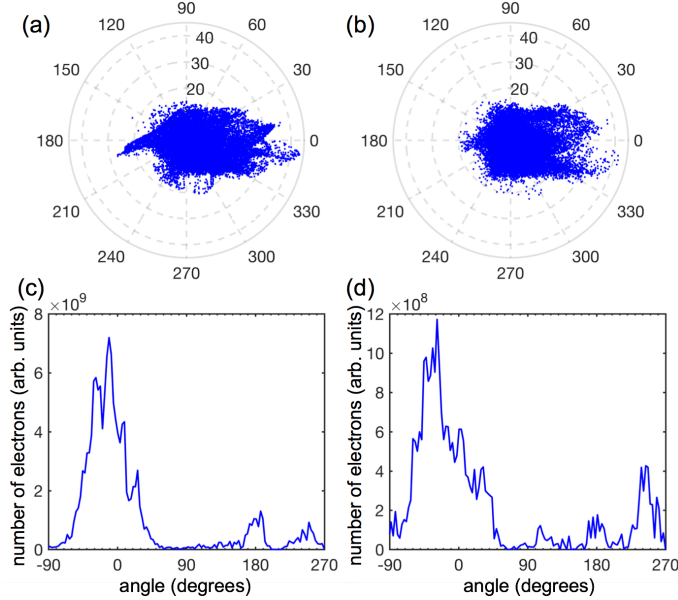


FIG. 3. (Color online.) (a) and (b) Distribution of electron divergence in the  $(\epsilon_e, \theta_{xy})$  polar plane from the 2D and 3D simulations, respectively, at  $t = 10T_0$ . Here,  $\epsilon_e = (\gamma - 1)m_e c^2$  and  $\theta_{xy} = \arctan(p_y/p_x)$ . (c) and (d) The corresponding angular distribution of the number of electrons with energies greater than 10 MeV.

and  $E_x^{(2D)} = 6 \times 10^{12}$  V/m and  $E_x^{(3D)} = 4 \times 10^{12}$  V/m at  $t = 35T_0$ . As a result, the proton energy from 3D simulation is lower than that from 2D. As shown in Fig. 2(f) for the proton energy spectrums, the MPE is 22 MeV in 3D and 43 MeV in 2D.

### III. QUALITATIVE MODEL ON PROTON ENERGY DIFFERENCE

As mentioned, it is of practical interest to find a relation between the MPEs obtained from the 2D and the more realistic 3D simulations. In this section, we investigate the dependence of the energy ratio on the laser and target parameters and give a qualitative model for this ratio.

The results are shown in Table I. The simulation setups in 2D and 3D are the same as that in Sec. II. The laser intensities are  $5 \times 10^{19}$  W/cm<sup>2</sup>,  $2 \times 10^{20}$  W/cm<sup>2</sup>, and  $1 \times 10^{21}$  W/cm<sup>2</sup>. For each intensity, two pulse durations, namely 20 fs and 100 fs, are investigated. It is found that the ratio between the resulting 2D and 3D MPEs is from 2 to 2.5 for laser spot radii from 3 to 4  $\mu$ m, respectively. That is, within the considered domain, the dependence on the

TABLE I. Comparison of maximum proton energies from 2D and 3D simulations for different laser and target parameters. The energy ratio given by the qualitative model is 2.17 for lasers with spot radius  $3 \mu\text{m}$ , and 2.51 for lasers with spot radius  $4 \mu\text{m}$ .

laser intensity	spot and duration	target thickness	proton energy (3D)	proton energy (2D)	energy ratio (2D/3D)
$5 \times 10^{19} \text{ W/cm}^2$	$3 \mu\text{m}$ , 20 fs	$1 \mu\text{m}$	4 MeV	8 MeV	2.00
$5 \times 10^{19} \text{ W/cm}^2$	$3 \mu\text{m}$ , 100 fs	$1 \mu\text{m}$	10 MeV	20 MeV	2.00
$2 \times 10^{20} \text{ W/cm}^2$	$4 \mu\text{m}$ , 20 fs	$1 \mu\text{m}$	9 MeV	21 MeV	2.33
$2 \times 10^{20} \text{ W/cm}^2$	$4 \mu\text{m}$ , 100 fs	$1 \mu\text{m}$	19 MeV	46 MeV	2.42
$1 \times 10^{21} \text{ W/cm}^2$	$3 \mu\text{m}$ , 20 fs	$1 \mu\text{m}$	22 MeV	43 MeV	1.95
$1 \times 10^{21} \text{ W/cm}^2$	$3 \mu\text{m}$ , 20 fs	$3 \mu\text{m}$	18 MeV	37 MeV	2.05
$1 \times 10^{21} \text{ W/cm}^2$	$3 \mu\text{m}$ , 20 fs	$6 \mu\text{m}$	16 MeV	33 MeV	2.06
$1 \times 10^{21} \text{ W/cm}^2$	$3 \mu\text{m}$ , 100 fs	$1 \mu\text{m}$	41 MeV	88 MeV	2.15

laser intensity is small. Moreover, the differences in the 2D and 3D MPEs for laser durations 20 fs and 100 fs are negligible. Simulations are also carried out for target thicknesses  $3 \mu\text{m}$  and  $6 \mu\text{m}$ , laser intensity  $1 \times 10^{21} \text{ W/cm}^2$ , pulse duration 20 fs, and spot radius  $3 \mu\text{m}$ . The results are also given in Table I. We see that, compared with that of the  $1 \mu\text{m}$  target, the proton energies for the target thicknesses  $3 \mu\text{m}$  and  $6 \mu\text{m}$  are less, which can be attributed to reduced electron recirculation inside the thicker target.<sup>27</sup> However, the corresponding 2D to 3D MPE ratios are about 2.05 and 2.06, which are near the value 1.95 for the  $1 \mu\text{m}$  target.

We now present a simple model for the 2D to 3D MPE ratio. We assume that the electron distribution in laser foil interaction is double Maxwellian, as shown in Fig. 2(b), where  $n(\epsilon) = n_{\text{cold}}(\epsilon) + n_{\text{hot}}(\epsilon) = \theta_{\text{cold}} \exp(-\epsilon/T_{\text{cold}}) + \theta_{\text{hot}} \exp(-\epsilon/T_{\text{hot}})$ . The cold electrons with energy less than 3 MeV contribute little to the sheath field since they are mostly reflected by the huge surface potential at the target rear. The hot electrons with energy larger than 3 MeV, as shown in Fig. 2(b), can be separated into two parts. The first part  $e1$ , which consists of electrons with energy higher than 3 MeV and lower than 10 MeV, is almost the same in the 2D and 3D simulations. The second part  $e2$ , which consists of electrons with energy greater than 10 MeV, is quite different in the 2D and 3D simulations. That is, the hot electrons can also be separated into two groups with different temperatures:  $n_{\text{hot}}(\epsilon) = \theta_{e1} \exp(-\epsilon/T_{e1}) + \theta_{e2} \exp(-\epsilon/T_{e2})$ . From Fig. 2(b), the fitted temperature for the  $e1$  electrons is the same in 2D and 3D cases with  $T_{e1}^{(2D)} \approx T_{e1}^{(3D)} \approx 2.4 \text{ MeV}$ . The temperature for the  $e2$  electrons is  $T_{e2}^{(2D)} \approx 4.2 \text{ MeV}$  in the 2D case and  $T_{e2}^{(3D)} \approx 1.9 \text{ MeV}$  in

the 3D case. The total number of hot electrons can be estimated from the energy relation  $N_{\text{total}} \sim \eta E_{\text{laser}} / \bar{\epsilon}_e$ , where  $N_{\text{total}}$  is the total number of hot electrons,  $\eta$  is the laser-electron energy conversion efficiency,  $E_{\text{laser}}$  is the input laser energy, and  $\bar{\epsilon}_e$  is the averaged electron kinetic energy. From the electron spectrums in Fig. 2(b), we find by integration over the spectrums that the total numbers of hot electrons with energy greater than 3 MeV is nearly equal in the 2D and 3D simulations, and the ratio is  $\frac{N_{\text{total}}^{(2D)}}{N_{\text{total}}^{(3D)}} \approx 1.05$ . The  $e2$  electrons only make up a small fraction of the total hot electrons. The fraction of the  $e2$  electrons is  $\frac{N_{e2}^{(2D)}}{N_{\text{total}}^{(2D)}} \approx 15\%$  in 2D and  $\frac{N_{e2}^{(3D)}}{N_{\text{total}}^{(3D)}} \approx 5\%$  in 3D. We can obtain from the energy spectrums the relation  $\sqrt{\frac{N_{e1}^{(2D)}T_{e1}^{(2D)} + N_{e2}^{(2D)}T_{e2}^{(2D)}}{N_{e1}^{(3D)}T_{e1}^{(3D)} + N_{e2}^{(3D)}T_{e2}^{(3D)}}} \approx 1.06$ , which shows that the laser-to-hot electron energy conversion efficiency in the 2D and 3D simulations is about the same.

The strength of the sheath electric field at the target rear surface can be approximated by  $E_{\text{sheath}} \sim T_e / e\lambda_D$ , where  $\lambda_D = \sqrt{\frac{\epsilon_0 T_e}{n_e e^2}}$  is the Debye length and here  $n_e$  is the hot electron density. The ratio of the sheath fields in 2D and 3D can then be expressed as

$$R_{\text{sheath}} = \frac{E_{\text{sheath}}^{(2D)}}{E_{\text{sheath}}^{(3D)}} \approx \sqrt{\frac{n_e^{(2D)} T_e^{(2D)}}{n_e^{(3D)} T_e^{(3D)}}} \approx \sqrt{\frac{\frac{N_{e1}^{(2D)}T_{e1}^{(2D)} + N_{e2}^{(2D)}T_{e2}^{(2D)}}{2\sigma}}{\frac{N_{e1}^{(3D)}T_{e1}^{(3D)} + N_{e2}^{(3D)}T_{e2}^{(3D)}}{\pi\sigma^2}}}. \quad (1)$$

From the calculations given in the above paragraph, we have obtained  $\sqrt{\frac{N_{e1}^{(2D)}T_{e1}^{(2D)} + N_{e2}^{(2D)}T_{e2}^{(2D)}}{N_{e1}^{(3D)}T_{e1}^{(3D)} + N_{e2}^{(3D)}T_{e2}^{(3D)}}} \approx 1$  by using the simulation data. Therefore,

$$R_{\text{sheath}} = \frac{E_{\text{sheath}}^{(2D)}}{E_{\text{sheath}}^{(3D)}} \approx \sqrt{\frac{\pi\sigma}{2}}. \quad (2)$$

The protons in the dot source at the target rear surface are accelerated by the sheath field, and their energy is  $\mathcal{E}_{\text{proton}} \approx e \int E_{\text{sheath}} ds_{\text{acc}}$ , where  $s_{\text{acc}}$  is the proton acceleration distance. In Eq. 2, the ratio of the sheath fields  $R_{\text{sheath}}$  is independent of the acceleration distance. Thus, the ratio of the 2D and 3D TNSA proton energies is then approximately

$$\frac{\mathcal{E}_{\text{proton}}^{(2D)}}{\mathcal{E}_{\text{proton}}^{(3D)}} \approx \frac{R_{\text{sheath}} \int E_{\text{sheath}}^{(3D)} ds_{\text{acc}}}{\int E_{\text{sheath}}^{(3D)} ds_{\text{acc}}} \approx \sqrt{\frac{\pi\sigma}{2}}, \quad (3)$$

where  $\sigma$  is the laser spot radius in units of  $\mu\text{m}$ . We see that the energy ratio depends on the laser spot radius, and it is 2.17 for  $\sigma = 3 \mu\text{m}$ , and 2.51 for  $\sigma = 4 \mu\text{m}$ . These estimated energy ratios agree fairly well with that obtained from the simulations, as can be seen in Table I.

TABLE II. Maximum proton energies from petawatt-picosecond laser-foil interactions.

laser intensity	spot and duration	preplasma length	target thickness	2D simulation results	corrected results	experiment results
$1 \times 10^{19}$ W/cm <sup>2</sup>	10 $\mu$ m, 1 ps	10 $\mu$ m	10 $\mu$ m	36 MeV	9 MeV	–
$5 \times 10^{19}$ W/cm <sup>2</sup>	10 $\mu$ m, 1 ps	10 $\mu$ m	10 $\mu$ m	82 MeV	21 MeV	–
$5 \times 10^{19}$ W/cm <sup>2</sup>	10 $\mu$ m, 1 ps	20 $\mu$ m	10 $\mu$ m	85 MeV	21 MeV	–
$5 \times 10^{19}$ W/cm <sup>2</sup>	10 $\mu$ m, 1 ps	80 $\mu$ m	10 $\mu$ m	95 MeV	23.8 MeV	23.2 MeV
$5.8 \times 10^{19}$ W/cm <sup>2</sup>	10 $\mu$ m, 1 ps	80 $\mu$ m	15 $\mu$ m	107 MeV	26.9 MeV	24.8 MeV
$7.2 \times 10^{19}$ W/cm <sup>2</sup>	10 $\mu$ m, 1 ps	80 $\mu$ m	15 $\mu$ m	113 MeV	28.3 MeV	29.1 MeV
$2 \times 10^{20}$ W/cm <sup>2</sup>	10 $\mu$ m, 1 ps	10 $\mu$ m	10 $\mu$ m	155 MeV	39 MeV	–

Our model is based on the assumption that the proton acceleration distance is the same in 2D and 3D. This is reasonable because in TNSA, the acceleration is mainly in the axial ( $x$ ) direction. Moreover, the protons gain energy within a few Debye lengths, where the sheath field is peaked near the target-vacuum interface.<sup>13,28</sup> After this effective acceleration region, the sheath field decays rapidly in all directions because of expansion of the hot electrons. However, the formula may not be applicable if the laser spot is large compared with the foil thickness. If we assume that the hot electron transport is ballistic,<sup>29</sup> the electron divergence effect can be neglected when the electron transverse displacement inside the foil is far less than the laser spot size, or  $d \cdot \tan \theta_{xy} / \sigma \ll 1$ , where  $d$  is the target thickness, and  $\theta_{xy}$  is the divergence angle. In this case, the proton acceleration would be roughly one dimensional, so that the TNSA proton energies from the 2D and 3D simulations would be similar. In the simulations of femtosecond laser-foil interactions in Sec. II, the hot electron (for electrons with energies greater than 10 MeV) divergence angles  $\theta_{xy}$  in the  $(x, y)$  plane is about 40° in 2D simulation and 50° in 3D simulation [see Figs. 3(c) and 3(d)]. Straightforward calculations show that  $d \cdot \tan \theta_{xy} / \sigma \approx 2/7$  in 2D and  $d \cdot \tan \theta_{xy} / \sigma \approx 2/5$  in 3D for target thickness 1  $\mu$ m and laser spot radius 3  $\mu$ m. These values suggest that multidimensional effects should be considered.

#### IV. PROTON ACCELERATION BY PETAWATT-PICOSECOND LASER

The results given in Table I demonstrate weak dependence of energy ratio on the laser pulse duration, thus it is possible to extend the qualitative model to estimate the proton energy in picosecond laser solid interactions. However, in picosecond laser plasma interac-

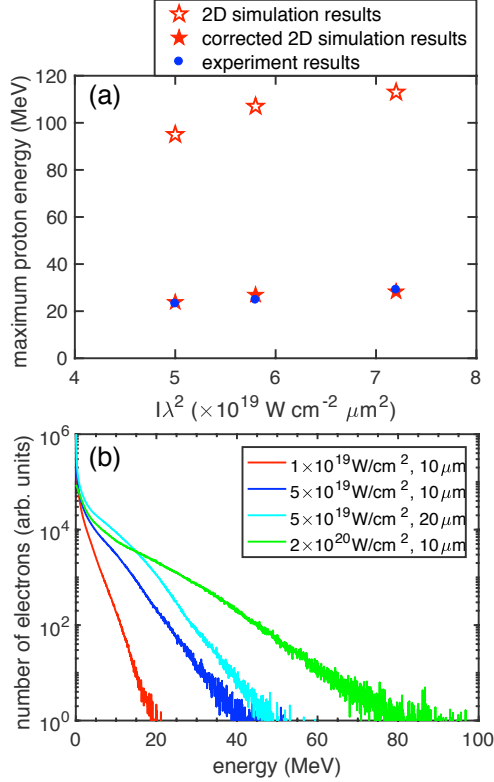


FIG. 4. (Color online) (a) Comparison of corrected simulation results and experiment results of MPE driven by petawatt-picosecond laser pulses. The blue dots are the experiment results from the SGII-U laser facility at Shanghai, China. The solid red stars are the corrected 2D simulation results by dividing the pristine 2D simulation results (shown in hollow red stars) by the energy ratio 3.96. The pristine and corrected 2D simulation results are shown in Table II. (b) Electron spectrums at  $t = 0.5$  ps for the simulated cases. The legend in (b) gives the laser intensity and preplasma length.

tions, a significant amount of preplasmas are usually generated by the irradiated prepulse prior to the arrival of the main pulse. To check the validity of the model, we have repeated the above simulations by considering two preplasma conditions.

In the first preplasma condition, a small preplasma is placed in front of the foil target, which corresponds to a high-contrast laser pulse. The preplasma density profile is  $n_e = n_0 \exp(x/l)$ , where  $l = 1 \mu\text{m}$  and the total preplasma length is  $10 \mu\text{m}$ . The flat foil target is composed of copper plasma with electron number density  $n_0 = 40n_c$ . The foil thickness and width are  $10 \mu\text{m}$  and  $34 \mu\text{m}$ , respectively. A plastic layer as proton source, of thickness  $0.5 \mu\text{m}$ , is attached to the foil rear surface. Three simulations for laser intensities  $1 \times$

$10^{19}$  W/cm<sup>2</sup>,  $5 \times 10^{19}$  W/cm<sup>2</sup>, and  $2 \times 10^{20}$  W/cm<sup>2</sup> are performed. The laser spot radius is  $10 \mu\text{m}$  and the laser pulse duration is 1 ps. The laser wavelength is  $1.06 \mu\text{m}$ . The simulation box ( $x \times y$ ) is  $180 \mu\text{m} \times 50 \mu\text{m}$  with the spatial grids  $6749 \times 1850$ , respectively. The corresponding grid length is 1 skin depth. The plastic layer is resolved by 19 spatial grids. In each plastic target cell, there are 50 electrons, 25 ions, and 1500 proton macroparticles.

The simulation results for the first preplasma condition are shown in Table II. The proton energies in 2D simulations for the laser intensities  $1 \times 10^{19}$  W/cm<sup>2</sup>,  $5 \times 10^{19}$  W/cm<sup>2</sup>, and  $2 \times 10^{20}$  W/cm<sup>2</sup> are 36 MeV, 82 MeV and 155 MeV, respectively. According to Eq. 3, the energy ratio is 3.96 for laser with spot radius  $10 \mu\text{m}$ . After dividing the 2D simulation results by the energy ratio, the corrected proton energies are 9 MeV, 21 MeV and 36 MeV, respectively. In view of the effects of preplasma length on proton acceleration, we have also carried out simulations with an  $l = 2 \mu\text{m}$  preplasma and total length  $20 \mu\text{m}$ . The laser intensity is  $5 \times 10^{19}$  W/cm<sup>2</sup>. In this case, one can see from Fig. 4(b) that the electron energy spectrum is similar to that of the  $10 \mu\text{m}$  preplasma. For the longer  $20 \mu\text{m}$  preplasma both the hot electron number and temperature are slightly higher than the  $10 \mu\text{m}$  preplasma, so that the TNSA proton energy (85 MeV vs. 82 MeV) is slightly higher than that of the shorter preplasma case.

In order to characterize more realistic experimental conditions of petawatt-picosecond laser facilities, three simulations are carried out using the laser parameters from the current laser facility SGII-U at Shanghai, China. The simulation and experimental results are also given in Table II. The laser intensity in each simulation is  $5.0 \times 10^{19}$  W/cm<sup>2</sup>,  $5.8 \times 10^{19}$  W/cm<sup>2</sup>, and  $7.2 \times 10^{19}$  W/cm<sup>2</sup>, respectively. The laser spatial profile is Gaussian, the laser duration is 1 ps, the laser spot radius is  $10 \mu\text{m}$ , and the laser wavelength is  $1.06 \mu\text{m}$ . A preplasma with  $l = 8 \mu\text{m}$  is assumed in the simulations, and the total preplasma length is  $80 \mu\text{m}$ . The width of the foil target is  $50 \mu\text{m}$ . The thickness of the foil target is  $10 \mu\text{m}$  and  $15 \mu\text{m}$  in the two cases. The target rear surface is coated with a plastic layer with thickness of  $0.5 \mu\text{m}$ . The simulation box is  $(x, y) = (290, 60) \mu\text{m}$  with a spatial grid of (10872, 2250). The corresponding grid length is 1 skin depth. The other simulation parameters are same as our picosecond laser simulations. For simulating such petawatt-picosecond laser experiments, a full 3D simulation is far beyond our computational resources, so that the 2D to 3D MPE ratio introduced here is useful.

In cases with long-scale preplasmas, the laser propagation in preplasma may be strongly

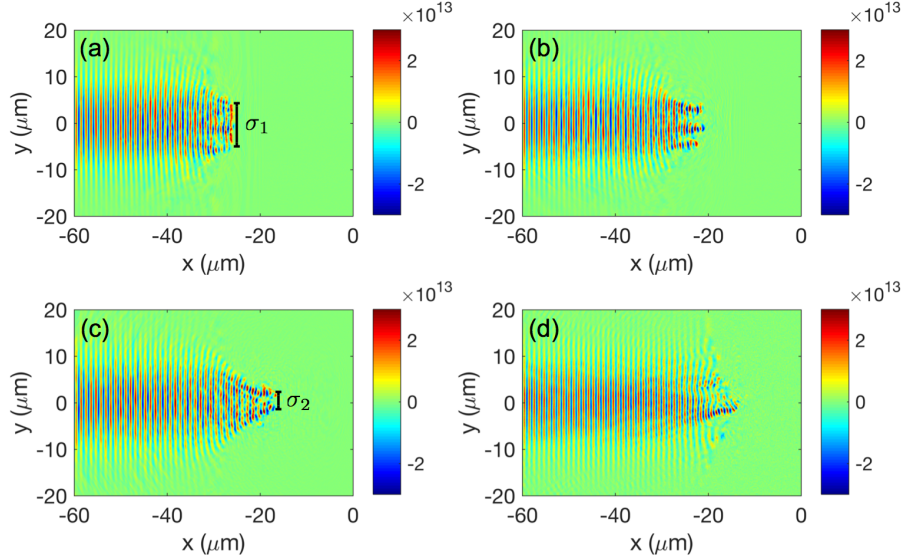


FIG. 5. (Color online.) Distribution of the laser electric field  $E_y$  in unit of V/m. (a) Snapshot at  $t = 60T_0$ , which is the time before the laser filamentation. The laser spot radius at this time is about  $\sigma_1 \approx 5 \mu\text{m}$ . (b) Snapshot at  $t = 70T_0$ , when the laser filamentation occurs. (c) Snapshot at  $t = 90T_0$ , when the laser filaments merge into one central beam. The laser beam spot radius at this time is about  $\sigma_2 \approx 2.5 \mu\text{m}$ . (d) Snapshot at  $t = 270T_0$ , which is the time close to 1 ps.

affected by the nonlinear instabilities, such as laser self-focusing, filamentation and hosing instability. These instabilities can change the laser spot in the preplasma. But the laser spot used in calculation of the energy ratio given in Eq. 3 is the vacuum spot radius. For example, Fig. 5 shows the laser propagation in the preplasma for the laser intensity  $5 \times 10^{19} \text{ W/cm}^2$ . We see in Fig. 5(a) that the laser spot radius changes from  $\sigma_0$  in vacuum to  $\sigma_1$ , and in Fig. 5(b) that modulation of the pulse front and filamentation of the laser occur. Fig. 5(c) shows that the laser pulse breaks up into several filaments,<sup>30,31</sup> and these filaments finally merge into one central beam at the later time. The laser spot radius at this time is denoted by  $\sigma_2$ . It is shown in Fig. 5 that the laser spot radius of  $\sigma_1$  is about  $5 \mu\text{m}$  and  $\sigma_2$  is about  $2.5 \mu\text{m}$ . From Eq. 3, we find that the energy ratios for  $\sigma_0$ ,  $\sigma_1$ , and  $\sigma_2$  are 3.96, 2.80, and 1.98, respectively. The MPE from the 2D simulation is 95 MeV. By dividing the energy ratios, the corrected proton energies for  $\sigma_0$ ,  $\sigma_1$ , and  $\sigma_2$  are 23.2 MeV, 33.9 MeV, and 47.9 MeV, respectively. We see that the result corresponding to the vacuum radius  $\sigma_0$  matches well with the experimental result 23.8 MeV, but the results corresponding to the self-focused lasers clearly over-estimate the proton energy.

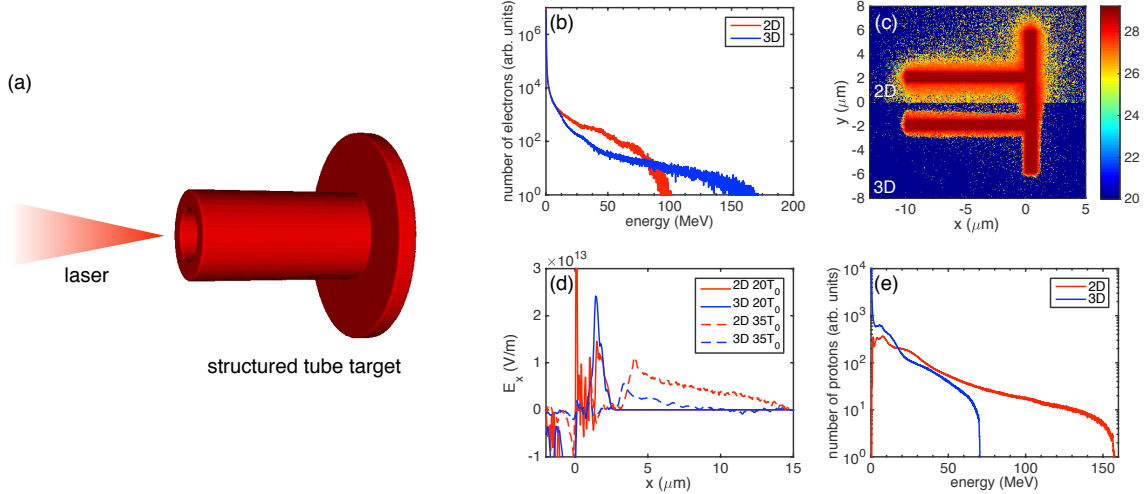


FIG. 6. (Color online) Simulation results for the structured tube target. (a) Target setup. (b) Electron spectrum at  $t = 30T_0$ . (c) Electron number density at  $t = 100T_0$ . (d) Profile of  $E_x$  at  $t = 20T_0$  and  $35T_0$ , respectively. (e) Proton spectrum at  $t = 100T_0$ .

From Table II, the proton energies in 2D simulations for the laser intensities  $5 \times 10^{19} \text{ W/cm}^2$ ,  $5.8 \times 10^{19} \text{ W/cm}^2$ , and  $7.2 \times 10^{19} \text{ W/cm}^2$  are 95 MeV, 107 MeV, and 113 MeV, respectively. After dividing the 2D simulation results by the energy ratio, the corrected proton energies are 23.8 MeV, 26.9 MeV, and 28.3 MeV, respectively. The experiment results are 23.2 MeV, 24.8 MeV, and 29.1 MeV, respectively. The corrected proton energy agrees fairly well with the experiment result.

Our result shows that by using 2D simulations, one can still predict the MPE in the picosecond laser-solid target experiments at the SGII-U laser facility. However, for picosecond laser pulses with lower contrast, larger scale preplasma will be generated and the laser pulse can be affected by the self-focusing, filamentation, and hosing instabilities. The TNSA of protons can then be affected, so that our empirical energy ratio may not be applicable.

## V. ENHANCEMENT OF PROTON ENERGY USING STRUCTURED TUBE TARGET

In this section, multidimensional effects on laser interaction with structured targets are investigated. Recently, many schemes have been proposed to enhance the TNSA accelerated proton energy by using the structured targets.<sup>23,24,32–42</sup> The cone structure has been included

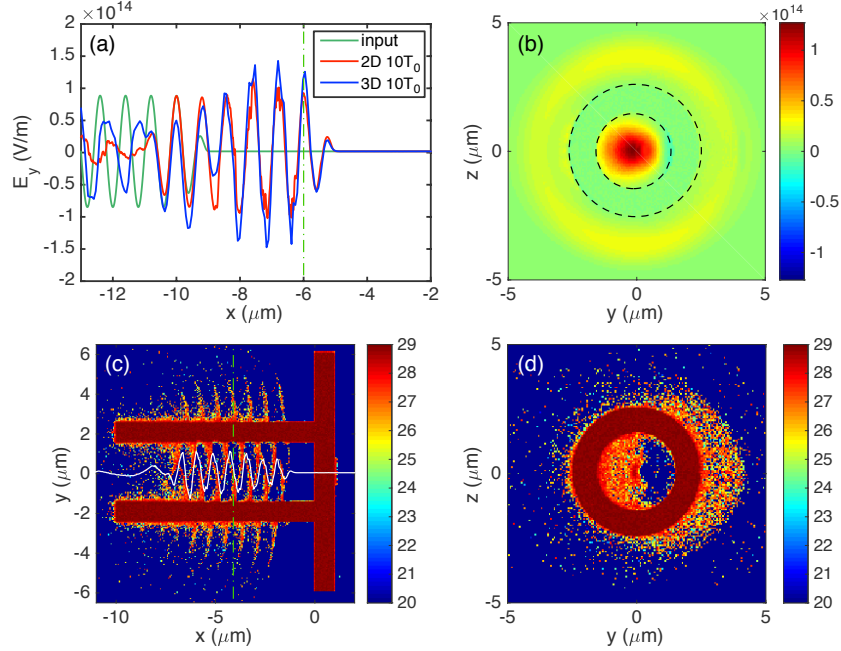


FIG. 7. (Color online) (a) Electric field  $E_y$  at  $t = 10T_0$  for 2D and 3D simulation results, respectively. (b) Transection of electric field  $E_y$  in 3D simulation at  $t = 10T_0$  and position  $x = -6 \mu\text{m}$ . (c) Electron number density and profile of the electric field  $E_y$  (white line) in 3D simulation at  $t = 15T_0$ . (d) Transection of electron number density at  $t = 15T_0$  and position  $x = -4 \mu\text{m}$ .

TABLE III. Comparison of maximum proton energy in 2D and 3D simulations for the structured tube targets. The cone-tube target is the structured tube target with an additional cone attached at the head of the plasma tube.

target structure	laser intensity	spot and duration	proton energy (3D)	proton energy (2D)	energy ratio (2D/3D)
cone-tube target	$2 \times 10^{20} \text{ W/cm}^2$	$4 \mu\text{m}$ , 30 fs	30 MeV	78 MeV	2.60
cone-tube target	$5 \times 10^{20} \text{ W/cm}^2$	$4 \mu\text{m}$ , 30 fs	62 MeV	153 MeV	2.46
structured tube target	$1 \times 10^{21} \text{ W/cm}^2$	$3 \mu\text{m}$ , 20 fs	71 MeV	156 MeV	2.19
structured tube target	$5 \times 10^{19} \text{ W/cm}^2$	$10 \mu\text{m}$ , 1 ps	–	167 MeV	–

in many target design, such as the slice-cone target<sup>43</sup>, the special designed target with two-stage acceleration<sup>44</sup>, etc. In our simulation, we proposed to use a straight tube target, which composed of a hollow cylinder plasma tube and a backside flat foil, as shown in Fig. 6 (a). Different from the cone target cases, in this scheme, the plasma tube acts as a waveguide. A periodic longitudinal electric field pattern is generated inside the tube and most of the electrons are effectively accelerated by this field. As a result, the proton energy is much

higher than the normal foil cases<sup>45</sup>.

In the simulation, the inner radius and thickness of the plasma tube are  $1.5 \mu\text{m}$  and  $1 \mu\text{m}$ , respectively. The thickness and width of the backside foil are  $1 \mu\text{m}$  and  $12 \mu\text{m}$ , respectively. Other simulation parameters are same as the simulations given in Sec. II. In simulation, the Gaussian laser irradiates from the left boundary of the simulation box and injects into the hollow plasma tube. In the tube, the laser is focused due to the optical confinement by the finite space inside the hollow tube. During focusing, the laser intensity is increased and the laser spot radius is reduced [see Figs. 7 (a) and 7 (b)]. The laser focusing in 2D and 3D simulations are compared. There is no  $z$  direction in the 2D simulations, thus the target in 2D is a planar object composed of two tube walls. The injected laser is focused only in the  $y$  direction by the upper and bottom tube walls. However, in the 3D simulation, the tube focuses the laser in the  $y$  and  $z$  directions simultaneously. A better laser optical focusing is obtained by the spatial symmetric cylinder tube [see Fig. 7 (b)]. When the laser injects into the tube, the laser  $E_y$  field pulls the electrons out of the tube walls. The pulled out electrons are then trapped and accelerated by the focused laser field. These electrons are kept in the laser accelerating phase for a long distance, comoving with the propagating field in the form of a series of electron bunches [see Figs. 7 (c) and 7 (d)]. The effective electron acceleration finally results in a higher electron temperature relative to the flat foil case in Sec. II [see Figs. 2 (b) and 6 (b)].

Due to the stronger focusing of the laser field in the 3D simulation, the electron maximum energy and high energy electron temperature (for electrons with energies greater than 20 MeV) in 3D simulation is higher than those in 2D [see Fig. 6(b)]. Hence, at the beginning, the sheath field strength in 3D is larger than that in 2D, which are  $E_x^{(3D)} = 2.5 \times 10^{13}$  V/m in 3D and  $E_x^{(2D)} = 1.2 \times 10^{13}$  V/m in 2D at  $t = 20T_0$ . However, in 3D, the electron divergence in the  $z$  direction results in lower trapping rate of the electrons pulled out by the laser field. The total high-energy electron number in the 3D simulation is less than that in 2D. [see Fig. 6(c)]. Moreover, in 3D simulation the electron divergence at the target backside also decreases the electron number density. Thus, at later times the sheath field strength in the 3D simulation decays rapidly and eventually lower than that in 2D. At  $t = 35T_0$ , the sheath field is  $E_x^{(3D)} = 0.5 \times 10^{13}$  V/m in 3D and  $E_x^{(2D)} = 1.0 \times 10^{13}$  V/m in 2D. The proton spectrum is shown in Fig. 6(e). The MPE in 3D is lower than that in 2D, which are 71 MeV in 3D and 156 MeV in 2D, respectively. The ratio of the 2D to 3D MPE is 2.19,

which agrees well with the value 2.17 from Eq. 3. Compared with the results given in Sec. II, the proton energy from the structured tube target is higher than that from the foil target for both 2D and 3D, due to the higher electron temperature in tube target. The simulation results for different laser and target parameters are listed in Table III. The cone-tube target is the structured tube target with an additional cone attached at the head of the plasma tube to increase the laser focusing<sup>45</sup>. It is shown that the energy ratio for structured tube target agrees with the qualitative model result given in Eq. 3.

To estimate the energy enhancement in petawatt-picosecond laser cases, a 2D simulation is performed. The target is composed of a plasma tube attached at the foil front surface with a small scale preplasma. The inner radius and thickness of the plasma tube are  $4 \mu\text{m}$  and  $2 \mu\text{m}$ , respectively. The length of the plasma tube is  $30 \mu\text{m}$ . The thickness and width for the backside foil are  $2 \mu\text{m}$  and  $34 \mu\text{m}$ , respectively. The target electron density is  $n_0 = 40n_c$ . The laser intensity is  $5 \times 10^{19} \text{ W/cm}^2$ , and its duration is 1 ps. The other simulation parameters are same as the simulations with first preplasma condition in Sec. IV. It is found that the MPE is 167 MeV in this 2D simulation. After dividing by the energy ratio of 3.96, the corrected proton energy would be 42 MeV. The proton energy from the structured tube target is about two times higher than the foil target.

## VI. SUMMARY

In summary, multidimensional effects on TNSA of protons have been investigated. Since the hot electron density and the induced sheath field at the target rear surface decrease more rapidly in 3D than that in 2D. The 2D simulations usually overestimate the MPE. Through both 2D and 3D simulations, a qualitative scaling law is established relating the MPEs obtained from the 2D and 3D simulations. It is demonstrated that the MPE ratio depends strongly on the laser spot size and displays weak dependence on the laser pulse durations, which make it feasible to estimate the MPE in picosecond laser solid interactions by only conducting the affordable 2D simulations. In addition, it is also applicable to estimate the MPE in laser structured target interactions by employing the energy ratio.

## ACKNOWLEDGMENTS

This work is supported by the National Key Program for S&T Research and Development, Grant No. 2016YFA0401100; the SSTDF, Grant No. JCYJ20160308093947132; the National Natural Science Foundation of China (NSFC), Grant Nos. 91230205, 11575031, and 11575298; the National Basic Research 973 Project, Grant No. 2013CBA01500. The EPOCH code was developed under the UK EPSRC Grant Nos. EP/G054940/1, EP/G055165/1, and EP/G056803/1. B.Q. acknowledges the support from Thousand Young Talents Program of China. We would like to thank that W. Wang presents us the experimental data done in the SGII-U laser facility in July 2017.

## REFERENCES

- <sup>1</sup>A. Macchi, M. Borghesi, and M. Passoni, *Rev. Mod. Phys.* 85, 751 (2013).
- <sup>2</sup>H. Daido, M. Nishiuchi, and A. S. Pirozhkov, *Rep. Prog. Phys.* 75, 056401 (2012).
- <sup>3</sup>A. P. L. Robinson, M. Zepf, S. Kar, R. G. Evans, and C. Bellei, *New J. Phys.* 10, 013021 (2008).
- <sup>4</sup>C. T. Zhou, and X. T. He, *Appl. Phys. Lett.* 90, 031503 (2007).
- <sup>5</sup>W. L. Zhang, B. Qiao, X. F. Shen, W. Y. You, T. W. Huang, X. Q. Yan, S. Z. Wu, C. T. Zhou, and X. T. He, *New J. Phys.* 18, 093029 (2016).
- <sup>6</sup>J. Bin, K. Allinger, W. Assmann, G. Dollinger, G. A. Drexler, A. A. Friedl, D. Habs, P. Hilz, R. Hoerlein, N. Humble, S. Karsch, K. Khrennikov, D. Kiefer, F. Krausz, W. Ma, D. Michalski, M. Molls, S. Raith, S. Reinhardt, B. Roper, T. E. Schmid, T. Tajima, J. Wenz, O. Zlobinskaya, J. Schreiber, and J. J. Wilkens, *Appl. Phys. Lett.* 101, 243701 (2012).
- <sup>7</sup>F. Abicht, J. Braenzel, G. Priebe, Ch. Koschitzki, A. A. Andreev, P. V. Nickles, W. Sandner, and M. Schnurer, *Appl. Phys. Lett.* 105, 034101 (2014).
- <sup>8</sup>X. T. He, J. W. Li, Z. F. Fan, L. F. Wang, J. Liu, K. Lan, J. F. Wu, and W. H. Ye, *Phys. Plasmas* 23, 082706 (2016).
- <sup>9</sup>M. Borghesi, J. Fuchs, S. V. Bulanov, A. J. MacKinnon, P. K. Patel, and M. Roth, *Fusion Sci. Technol.* 49, 412 (2006).
- <sup>10</sup>M. Passoni, L. Bertagna, and A. Zani, *New J. Phys.* 12, 045012 (2010).

- <sup>11</sup>S. C. Wilks, A. B. Langdon, T. E. Cowan, M. Roth, M. Singh, S. Hatchett, M. H. Key, D. Pennington, A. MacKinnon, and R. A. Snavely, *Phys. Plasmas* 8, 542 (2001).
- <sup>12</sup>P. Mora, *Phys. Rev. Lett.* 90, 185002 (2003).
- <sup>13</sup>R. A. Snavely, M. H. Key, S. P. Hatchett, T. E. Cowan, M. Roth, T. W. Phillips, M. A. Stoyer, E. A. Henry, T. C. Sangster, M. S. Singh, S. C. Wilks, A. MacKinnon, A. Offenberger, D. M. Pennington, K. Yasuike, A. B. Langdon, B. F. Lasinski, J. Johnson, M. D. Perry, and E. M. Campbell, *Phys. Rev. Lett.* 85, 2945 (2000).
- <sup>14</sup>S. A. Gaillard, T. Kluge, K. A. Flippo, M. Bussmann, B. Gall, T. Lockard, M. Geissel, D. T. Offermann, M. Schollmeier, Y. Sentoku, and T. E. Cowan, *Phys. Plasmas* 18, 056710 (2011).
- <sup>15</sup>F. Wagner, O. Deppert, C. Brabetz, P. Fiala, A. Kleinschmidt, P. Poth, V. A. Schanz, A. Tebartz, B. Zielbauer, M. Roth, T. Stöhlker, and V. Bagnoud, *Phys. Rev. Lett.* 116, 205002 (2016).
- <sup>16</sup>J. Fuchs, P. Antici, E. d’Humières, E. Lefebvre, M. Borghesi, E. Brambrink, C. A. Cecchetti, M. Kaluza, V. Malka, M. Manclossi, S. Meyroneinc, P. Mora, J. Schreiber, T. Toncian, H. Pépin, and P. Audebert, *Nat. Phys.* 2, 48–54 (2006).
- <sup>17</sup>L. Robson, P. T. Simpson, R. J. Clarke, K. W. D. Ledingham, F. Lindau, O. Lundh, T. McCanny, P. Mora, D. Needly, C.-G. Wahlström, M. Zepf, and P. McKenna, *Nat. Phys.* 3, 58–62 (2007).
- <sup>18</sup>A. Sgattoni, P. Londrillo, A. Macchi, and M. Passoni, *Phys. Rev. E* 85, 036405 (2012).
- <sup>19</sup>E. d’Humières, A. Brantov, V. Yu. Bychenkov, and V. T. Tikhonchuk, *Phys. Plasmas* 20, 023103 (2013).
- <sup>20</sup>J. L. Liu, M. Chen, J. Zheng, Z. M. Sheng, and C. S. Liu, *Phys. Plasmas* 20, 063107 (2013).
- <sup>21</sup>M. Blanco, M. T. Flores-Arias, C. Ruiz, and M Vranic, *New J. Phys.* 19, 033004 (2017).
- <sup>22</sup>T. D. Arber, K. Bennett, C. S. Brady, A. Lawrence-Douglas, M. G. Ramsay, N. J. Sircobe, P. Gillies, R. G. Evans, H. Schmitz, A. R. Bell, and C. P. Ridgers, *Plasma Phys. Controlled Fusion* 57, 113001 (2015).
- <sup>23</sup>H. Schwoerer, S. Pfoth, O. Jackel, K.-U. Amthor, B. Liesfeld, W. Ziegler, R. Sauerbrey, K. W. D. Ledingham, and T. Esirkepov, *Nature* 439, 445–448 (2006).
- <sup>24</sup>A. P. L Robinson, and P. Gibbon, *Phys. Rev. E* 75, 015401(R) (2007).
- <sup>25</sup>P. Gibbon, *Phys. Rev. E* 72, 026411 (2005).

- <sup>26</sup>A. Pukhov, Phys. Rev. Lett. 86, 3562 (2001).
- <sup>27</sup>A. J. Mackinnon, Y. Sentoku, P. K. Patel, D. W. Price, S. Hatchett, M. H. Key, C. Andersen, R. Snavely, and R. R. Freeman, Phys. Rev. Lett. 88, 215006 (2002).
- <sup>28</sup>M. Passoni, V. T. Tikhonchuk, M. Lontano, and V. Yu. Bychenkov, Phys. Rev. E 69, 026411 (2004).
- <sup>29</sup>M. Coury, D. C. Carroll, A. P. L. Robinson, X. H. Yuan, C. M. Brenner, M. Burza, R. J. Gray, M. N. Quinn, K. L. Lancaster, Y. T. Li, X. X. Lin, O. Tresca, C.-G. Wahlström, D. Neely, and P. McKenna, Appl. Phys. Lett. 100, 074105 (2012).
- <sup>30</sup>A. Pukhov, and J. Meyer-ter-Vehn, Phys. Rev. Lett. 76, 3975 (1996).
- <sup>31</sup>T. W. Huang, C. T. Zhou, A. P. L. Robinson, B. Qiao, H. Zhang, S. Z. Wu, H. B. Zhuo, P. A. Norreys, and X. T. He, Phys. Rev. E 92, 053106 (2015).
- <sup>32</sup>T. Toncian, M. Borghesi, J. Fuchs, E. d’Humières, P. Antici, P. Audebert, E. Brambrink, C. A. Cecchetti, A. Pipahl, L. Romagnani, and O. Willi, Science 312, 410–413 (2006).
- <sup>33</sup>T. Bartal, M. E. Foord, C. Bellei, M. H. Key, K. A. Flippo, S. A. Gaillard, D. T. Offermann, P. K. Patel, L. C. Jarrott, D. P. Higginson, M. Roth, A. Otten, D. Kraus, R. B. Stephens, H. S. McLean, E. M. Giraldez, M. S. Wei, D. C. Gautier, and F. N. Beg, Nat. Phys. 8, 139–142 (2012).
- <sup>34</sup>T. Kluge, S. A. Gaillard, K. A. Flippo, T. Burris-Mog, W. Enghardt, B. Gall, M. Geissel, A. Helm, S. D. Kraft, T. Lockard, J. Metzkes, D. T. Offermann, M. Schollmeier, U. Schramm, K. Zeil, M. Bussmann, and T. E. Cowan, New J. Phys. 14, 023038 (2012).
- <sup>35</sup>B. Qiao, M. E. Foord, M. S. Wei, R. B. Stephens, M. H. Key, H. McLean, P. K. Patel, and F. N. Beg, Phys. Rev. E 87, 013108 (2013).
- <sup>36</sup>C. T. Zhou, L. Y. Chew, and X. T. He, Appl. Phys. Lett. 97, 051502 (2010). C. T. Zhou, and X. T. He, Opt. Lett. 32, 2444 (2007).
- <sup>37</sup>K. D. Xiao, C. T. Zhou, B. Qiao, and X. T. He, Phys. Plasmas 22, 093112 (2015).
- <sup>38</sup>L. L. Ji, J. Snyder, A. Pukhov, R. R. Freeman, and K. U. Akli, Sci. Reports 6, 23256 (2016).
- <sup>39</sup>S. Jiang, L. L. Ji, H. Audesirk, K. M. George, J. Snyder, A. Krygier, P. Poole, C. Willis, R. Daskalova, E. Chowdhury, N. S. Lewis, D. W. Schumacher, A. Pukhov, R. R. Freeman, and K. U. Akli, Phys. Rev. Lett. 116, 085002 (2016).
- <sup>40</sup>L. Yi, A. Pukhov, P. L. Thanh, and B. Shen, Phys. Rev. Lett. 116, 115001 (2016).
- <sup>41</sup>Z. Léczy, and A. Andreev, Phys. Rev. E 93, 013207 (2016).

- <sup>42</sup>L. Hu, T. Yu, F. Shao, D. Zou, and Y. Yin, *Phys. Plasmas* 22, 033104 (2015).
- <sup>43</sup>J. Zheng, Z. M. Sheng, J. L. Liu, W. M. Zhou, H. Xu, and J. Zhang, *Phys. Plasmas* 18, 113103 (2011).
- <sup>44</sup>J. L. Liu, Z. M. Sheng, J. Zheng, W. M. Wang, M. Y. Yu, C. S. Liu, W. B. Mori, and J. Zhang, *Phys. Rev. ST-AB*, 15, 101301 (2012).
- <sup>45</sup>K. D. Xiao, T. W. Huang, C. T. Zhou, B. Qiao, S. Z. Wu, S. C. Ruan, and X. T. He, *AIP Advances* 6, 015303 (2016). K. D. Xiao, T. W. Huang, L. B. Ju, R. Li, S. L. Yang, Y. C. Yang, S. Z. Wu, H. Zhang, B. Qiao, S. C. Ruan, C. T. Zhou, and X. T. He, *Phys. Rev. E* 93, 043207 (2016).